A Study of the Mechanism for Globular Metal Transfer from Covered Electrodes

Through the use of high-speed photography, a systematic analysis of the globular droplet was made, and a mechanism of transfer is proposed

BY J. H. CHEN, D. FAN, Z. Q. HE, J. YE AND Y. C. LUO

ABSTRACT. In this investigation, arc force, surface tension and the statistical sizes of drops transferred from covered electrodes were measured. By means of x-ray photography and a laser high-speed camera that recorded two images in synchronization with the arc sound and voltage signals, the observation of transfer modes and the measurements of oscillatory parameters of metal drops were carried out. On the basis of these results, mechanical factors affecting transfer were analyzed quantitatively and systematically. Thus, a mechanism of globular metal transfer from covered electrodes is offered.

Introduction

In spite of the importance of investigating the metal transfer from covered electrodes, there has been little work devoted to the systematical and quantitative analysis of mechanical factors affecting this process. The mechanism of metal transfer from covered electrodes was investigated mainly on the basis of phenomenal observation. The meagerness of work in this area is because the forces affecting metal transfer during manual shielded metal arc welding, such as arc force, surface tension and the force caused by the oscillation of the drop, are difficult to measure and the tip of the electrode is always hidden by a deep cavity formed by the covering.

KEY WORDS

Metal Transfer
Transfer Mechanism
Globular Metal
Globular Transfer
Covered Electrodes
Drop Oscillation
Shielded Metal Arc
SMA Welding
Laser Photography
X-ray Photography

J. H. CHEN is a Professor and President; D. FAN, Z. Q. HE and J. YE are Lecturers; and Y. C. LUO is an Assistant at Gansu University of Technology, Lanzhou, China.

In this work, the authors used a special purpose apparatus to measure arc force, surface tension and the statistical sizes of drops transferred from covered electrodes. The modes of metal transfer were observed by means of x-ray photography and laser high-speed photography equipment that recorded two images in synchronization with the arc sound and voltage signals. From the measured parameters, the inertial forces caused by oscillation of the drops were estimated. On the basis of the above results and the analysis of mechanical factors, a mechanism of globular metal transfer was proposed.

Description of Experiment

Materials

Mild steel plates with dimensions of 300 × 40 × 10 mm (12 × 1.6 × 0.4 in.) were used as test pieces. 309 stainless steel (C < 0.08%, Si < 1.0%, Mn < 2.0%, Ni 12.0–14.0%, Cr 22.0–24.0%, P < 0.04%, S < 0.03%) wire 4 mm (0.16 in.) in diameter was used as the core wire. Initial composition of the covering consisted of rutile (60%), titanium dioxide (5%), iron powder (24%) and soda (2%), with sodium silicate as a binder. By substituting marble (0–50%), feldspar (0–50%) and fluorspar (0–20%), respectively, for equivalent rutile, three series of 16 batches of test electrodes were prepared for the experiments. In addition, commercial basic electrodes 4 mm in diameter were used as well.

Procedure

All experiments were carried out with welding conditions of 150 A, DCEP (reverse polarity), and in the flat position; however, in some instances, the current was varied as indicated by values shown in Figs. 6 and 9. The apparatus for the laser high-speed photography is shown schematically in Fig. 1. Through focusing and filter lenses, apertures, and an optical fiber, the image of the metal drop was projected onto the main lens of the high-speed camera by laser backlight. The side image of the arc was also taken by the main lens through another optical fiber. The arc sound was transferred to electric signals by the microphone and the amplifier with a band-pass filter and was inputted to the light oscillograph with the signals of arc voltage. The oscillograms were taken into the side lens of the high-speed camera. With this apparatus, four events — the metal drop image, the arc side image, the arc sound and the arc voltage — could be recorded in one frame of film taken at the speed of 1000–2000 f/s.

The apparatus for the x-ray high-speed photography is shown schematically in Fig. 2. The metal drop silhouette was projected onto the input screen of the image magnifier by continuous x-ray. The image formed on the input screen was converted on the output screen to a one-tenth size greenish-yellow image having a 1000 times higher intensity. This image was photographed by the high-

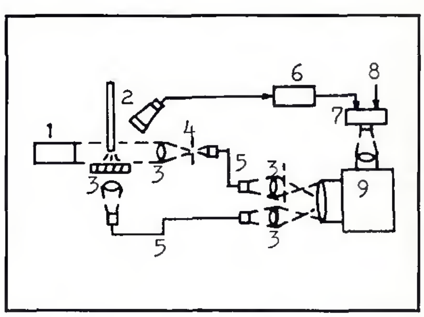

Fig. 1 — Schematic illustration of the apparatus for high-speed photography that records two images sychronized with the arc sound and voltage signals. 1 — Laser back light; 2 — microphone; 3 — lens; 4 — aperture; 5 — optical fiber; 6 — magnifier with band filter; 7 — light oscillograph; 8 — arc voltage signal; 9 — high-speed camera

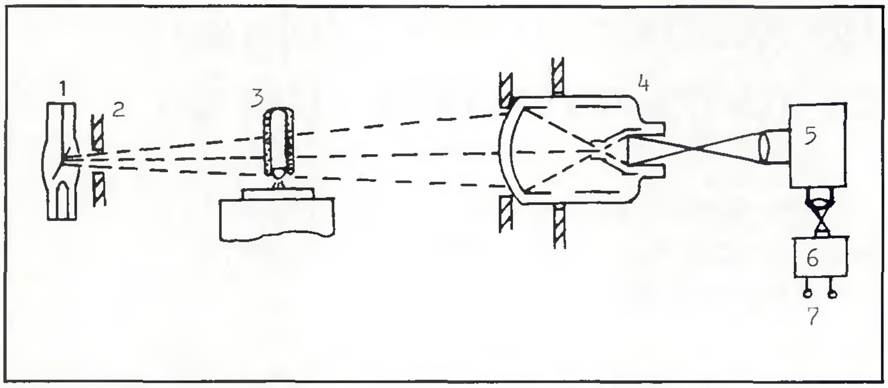

Fig. 2 — Schematic illustration of the apparatus for x-ray high-speed photography. 1 — X-ray tube; 2 — lead shield; 3 — electrode; 4 — image magnifier; 5 — high-speed camera; 6 — light oscillograph; 7 — signals; 8 — lens

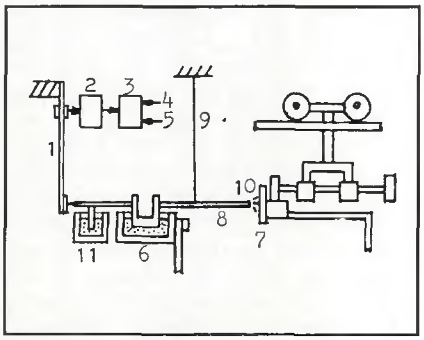

Fig. 3 — Schematic illustration of apparatus for measuring arc pressure. 1 — Force sensor; 2 — strainometer; 3 — recorder; 4 — arc voltage signal; 5 — arc current signal; 6 — mercury pool; 7 — plate specimen; 8 — electrode; 9 — wire for suspending electrode; 10 — arc; 11 — oil damper

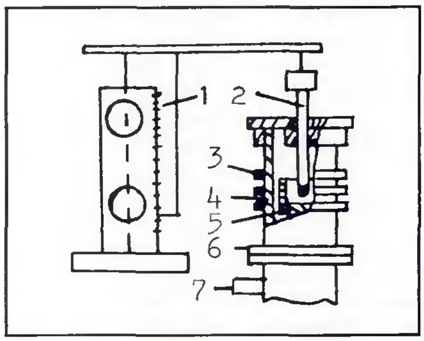

Fig. 4 — Schematic illustration of the apparatus for measuring surface tension. 1 — Elevator mechanism; 2 — electrode; 3 — induction coil; 4 — silica tube; 5 — graphite crucible; 6 — pump; 7 — argon inlet

speed camera after optical magnification. The arc voltage signals were synchronously taken from the light oscillograph by the side lens of the high-speed camera.

The following conditions were used for the photography: an x-ray tube current of 4 mA; accelerating voltage of 80 kV; target size of 0.4 × 0.4 mm; and a frame speed of 250-400 f/s. The resolving power for static images reached 0.2 mm (steel penetrator). The apparatus for measuring arc force was a modification of the one used by Conn (Ref. 1) and shown schematically in Fig. 3. In order to reduce the frictional resistance to a minimum, the electrode was floated on mercury at one end and suspended by a thin wire in the middle. Through the mercury coupling, a constant current power source supplied the welding current. The arc burned between the other end of the electrode and a rotated plate. Through the sensor and strainometer, the reaction of the average arc force, which acted on the electrode, was transferred to electrical signals and recorded by a pen recorder in synchronization with the signals of the arc voltage and current.

The apparatus for measuring the surface tension of the melted metal drop is shown schematically in Fig. 4. The electrode, with a thin layer of covering, was attached to the elevator at one end, and the other end extended down into the graphite crucible. This was heated by high-frequency current in a quartz tube evacuated and charged with argon. By lowering the electrode slowly, the melted drop at its tip got bigger and bigger until it could not be suspended by the surface tension, and it dropped down. From the critical weight of the drop, the coefficient of surface tension can be calculated by the following equation (Ref. 2):

$$\sigma = \frac{mg}{r} F \qquad (1)$$

Where σ = coefficient of surface tension (dyn/cm); mg = critical drop weight (dyn); r = radius of core wire (cm); and F = coefficient.

Though the measured coefficient of surface tension was equal to the value at the temperature near melting point, the pattern of the drop was similar to that produced during welding.

Statistical sizes of drops transferred from covered electrodes were measured as d_{50} by the method suggested by Ishizaki (Ref. 3). The d_{50} is the statistical diameter of drops corresponding to 50% integral weight of all drops.

Experimental Results

Results of Arc Pressure Measurements

The dependence of arc force produced during welding on the content of various components in the covering is plotted in Fig. 5. It was shown that with increasing marble content, arc force increased markedly. In the range of 0-50% of feldspar content, the arc force varied slightly.

Figure 6 shows the arc force produced during welding at different currents with basic electrodes baked at various temperatures for 4 h. It was found that arc force increased approximately with the square of welding current and decreased with increasing baking temperature. Arc force of the electrodes baked at 700°C (1292°F) for 4 h is about one-third of that in the unbaked condition.

Results of Surface Tension Measurements

The surface tension coefficients of HO8A mild steel and Type 309 stainless steel core wires measured in argon were 1433 dyn/cm and 1522 dyn/cm, respec-

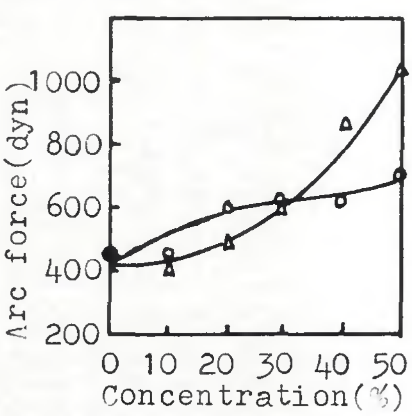

Fig. 5 — Relationship between arc force and composition of the covering: △ marble; o feldspar

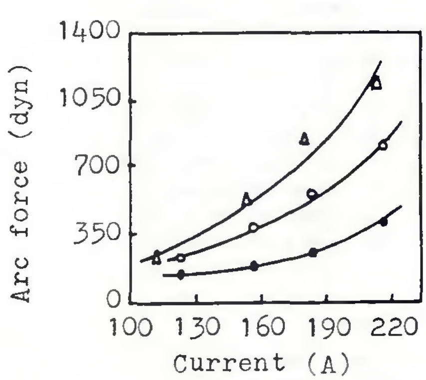

Fig. 6 — Arc force of electrodes baked at different temperatures and welded with different currents: △ unbaked condition; o 450°C; • 700°C

tively. The coefficients of surface tension of the melted drops as a function of the contents of the various components in the covering are plotted in Fig. 7. Figure 7 shows that as the marble in the covering increased, the surface tension increased remarkably. In the range up to 20% fluorspar, surface tension increased; however, feldspar decreased it.

Results of Measurements of Statistical Sizes of Drops d_{50}

The relationship between d_{50} and the content of various components in the covering is plotted in Fig. 8. It was found that statistical sizes of drops increased uniformly with an increase of fluorspar in the covering. However, drop size decreased with increasing concentrations of feldspar. In the case of marble additions, d_{50} increased markedly with levels up to 10%, but thereafter decreased remarkably.

The statistical sizes of drops produced during welding with commercial basic electrodes at different currents are shown in Fig. 9, and those produced with electrodes baked at different temperatures are shown in Fig. 10. The same figures show the corresponding arc force as well.

Results of High-Speed Photography

Figure 11A shows a typical sample of the photos taken by the laser high-speed photography equipment that recorded two images while synchronizing arc sound and voltage signals. On the left side of the photo is a sequential series of images of the drop. Side images of the arc appear on the right as a series of bright spots. The curved line on the right represents arc sound signals, and the line next to it on the left represents arc voltage signals. The four frames at the top show a short circuit of the electrode to the pool. In this duration, side images of the arc disappeared, the voltage was low and arc sound signals were more stable. In the fifth frame, the arc reignited. At this moment, arc voltage increased abruptly, side image appeared and arc sound signals became more violent.

Figure 11B shows the magnified photo taken by x-ray high-speed photography. In this figure, the process of detachment of the melted metal drop from the tip of the covered electrode is shown in detail, and the covering can be distinguished from the core wire.

Figure 12 consists of one set of photos showing the oscillating movement of the melted metal drops at the tip of the electrodes. In Fig. 12A, the eighth frame from the top shows that the drop reached the lowest position but without a short circuit because the side image of the arc still appeared on the right. From the ninth frame, the drop moved upward and reached the highest position in the 19th frame after about 22 ms.

Figures 12B and C, which were taken by x-ray high-speed photography, show the oscillatory movement of the drops before detachment. The period was about 40-50 ms. Fig. 12D shows the oscillogram of current and voltage during welding. Arc voltage oscillated within the same time period (40-50 ms) as the metal drop oscillation. The amplitude of the oscillation increased with the growth of the drop. Most of the drops transferred just at the trough of oscillation.

Figure 13 shows the relationship between the moment of drop detachment and the jump in arc voltage as represented by the jump of the arc spot. In most cases, arc spots jumped simultaneously with or very close to drop detachment.

Figure 14 shows the mechanism of transfer as a lateral pressure by the arc force on the drop, which occurred only in exceptional cases, such as with eccentric covered electrodes.

Figure 15 illustrates the phenomenon of double arcs. From the fourth frame, the arc voltage increased abruptly, and on the left, the image of double arcs

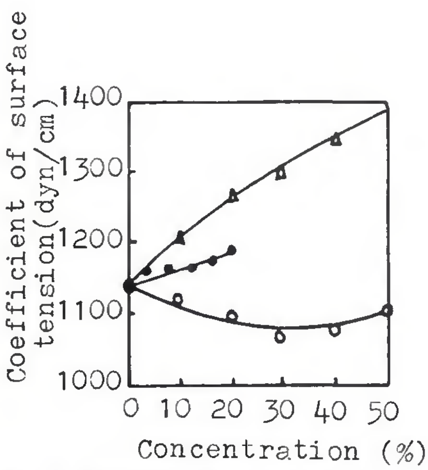

Fig. 7—Relationship between coefficient of surface tension and composition of covering: △ marble; ○ feldspar; ● fluorspar

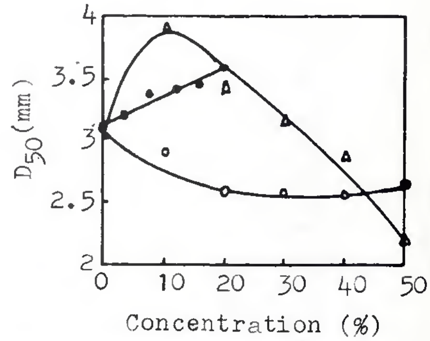

Fig. 8—Relationship between d_{50} and composition of covering: △ marble; ○ feldspar; ● fluorspar

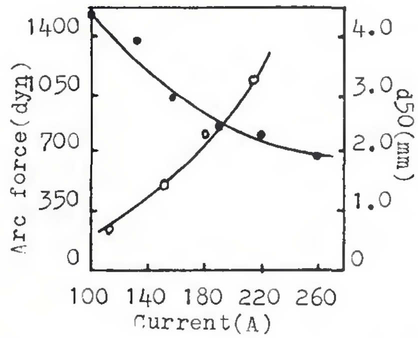

Fig. 9—d_{50} and arc force produced in welding with basic electrodes with different currents: ● d_{50}; ○ arc force

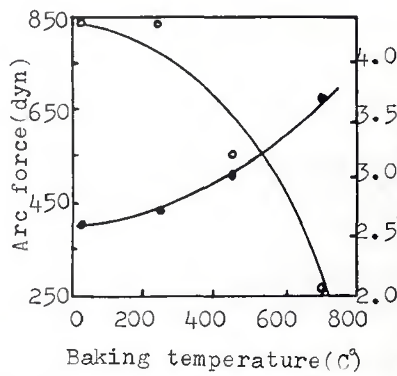

Fig. 10—Statistical sizes of drops d_{50} and arc pressure produced with basic electrodes baked at various temperatures: ● d_{50}; ○ arc pressure

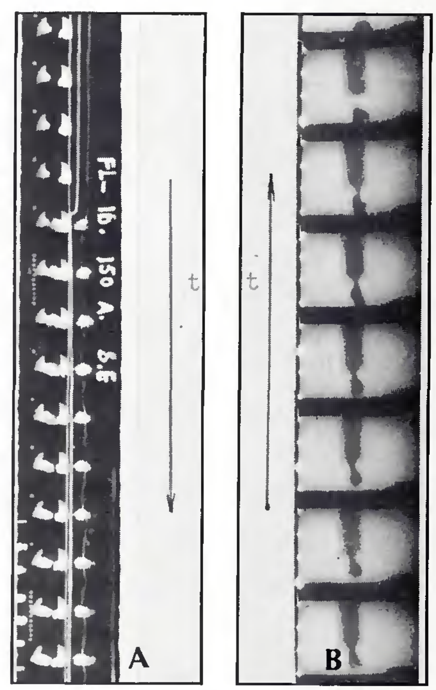

Fig. 11—Typical samples of photos taken by: A—Laser high-speed photography that recorded two images synchronized with arc sound and voltage signals (1000 f/s); B—x-ray high-speed photography (250 f/s)

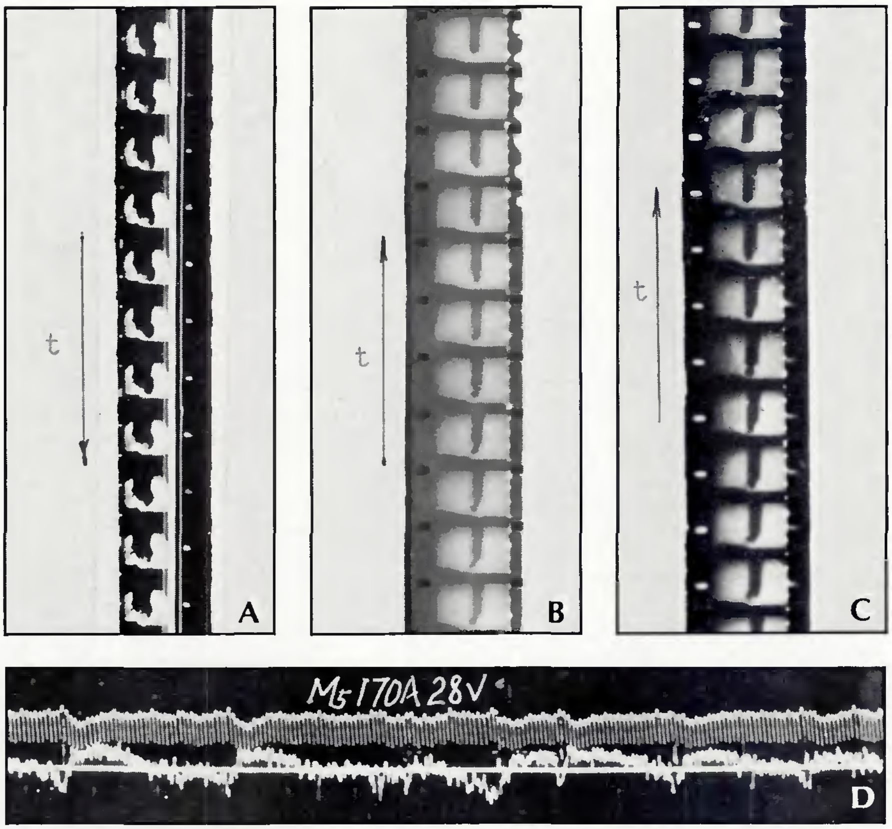

Fig. 12 — Oscillation of melted metal drops before detachment. A — Laser high-speed photography (500 f/s); B and C — x-ray high-speed photograph (250 f/s); D — oscillogram of welding current (top) and voltage (bottom) 200 mm/s

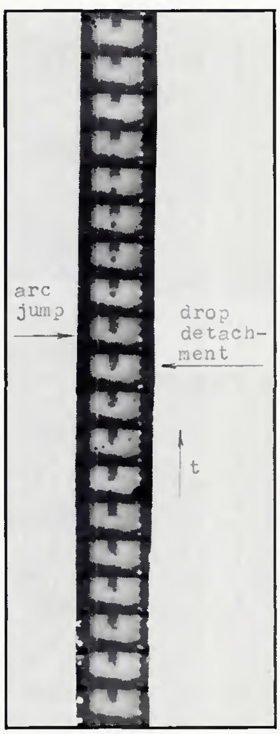

Fig. 13 — X-ray high-speed photograph showing the moment of drop detachment and the jump of the arc (250 f/s)

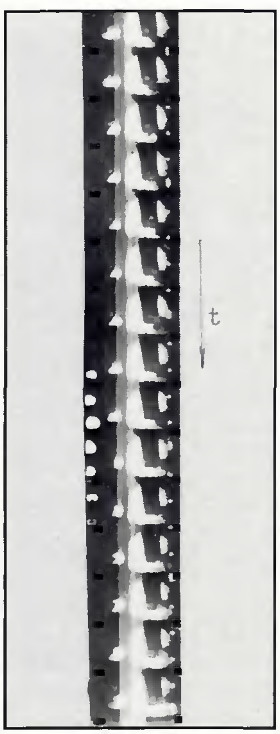

Fig. 14 — Laser high-speed photograph showing the lateral pressure of arc on the drop (500 f/s)

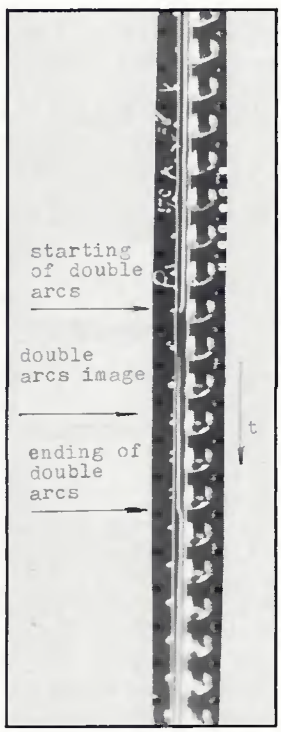

Fig. 15 — Laser high-speed photograph showing the double-arc phenomenon (1000 f/s)

appeared. At the tenth frame, the arc voltage returned to normal value and the image of double arcs disappeared.

Discussion

Effect of Surface Tension

It is well known that surface tension, which acts as the main force prohibiting the drop from transferring, is one of the principal factors that control the process of metal transfer. In this investigation, the relationship of the statistical drop sizes and surface tension of the drops correlated well with various contents of fluorspar and feldspar — Fig. 16. Surface tension tended to control drop size.

Source and Effect of Arc Force

It was indicated in Fig. 6 that the arc force of the basic eletrode baked at 700°C was cut down to 30% of that in the unbaked condition. Considering that this remaining force still included the pressure produced by vapor and evolved gas, it was reasonable to conclude that arc force originated mainly from gases evolved from decomposition of carbonates and vapors evaporated from the wire and the covering. Supplementary experiments revealed that the increment of the arc force was approximately in proportion to the square increment of the quantity of gas evolved from the marble in the covering. The force originated from other sources, such as electromagnetic effect, was smaller.

Effect of Arc Force

It was shown in Fig. 17A that the surface tension increased uniformly with the marble content in the covering, but the d_{50} reached a maximum at the point of 10% marble content and then decreased sharply. This fact drew attention to the effect of the arc force. Figure 17B shows the relationship between the difference of force calculated by substracting arc force from surface tension, and the statistical weight of the drops of the electrodes with various marble contents. As this figure indicates, the trend of these two curves is similar in pattern. From Figs. 9 and 10, it was seen that the decrease in the drop sizes, with a corresponding increase in welding current and a decrease in baking temperature, could be attributed to the increase of arc force. Moreover, these facts establish the important effect of arc force on drop detachment.

Effect of Inertial Force Induced by Oscillation of the Melted Metal Drop

In Fig. 17, the curve showing the relationship of the statistical weight of the drops of the electrodes with various marble contents has a similar trend with that of the difference of the forces calculated by subtracting arc force from surface tension, but there were about 300 dyn difference between these two curves for drops with a weight more than 100 dyn. This result meant that in order to overcome the surface tension and detach a drop from the electrode, there must be a force of about 300 dyn to join the arc force and the drop weight. On the other hand, in Fig. 12, high-speed photographs show the oscillation of the metal drop before detachment. Using the measured frequency, the amplitude of oscillation, and the mass of the metal drop, the inertial force induced by oscillation could be calculated. For simplicity, calculation was carried out on the supposition that the oscillation of the metal drop took the simple harmonic vibration pattern. In this case, the inertial force could be calculated by the following equation:

$$Y = A \sin Wt$$

$$a = \frac{d^2y}{dt^2} = -AW^2 \sin Wt$$

at the lowest position

$$a = -AW^2$$

$$F = -ma = mAW^2 = mA(2\pi f)^2$$

where F = inertial force induced by oscillation; m = mass of metal drop; a = acceleration in oscillation; W = frequency of oscillation in angle; f = frequency of oscillation.

This inertial force acted to detach the drop from the electrode. For the basic electrodes, measured values of A and f were in the range of 1.0–1.7 mm and 20–45/s, respectively. Using corresponding data and the statistical drop mass of 0.1 g, the calculated F was about 300 dyn. These data indicate that the inertial force induced by oscillation is an important mechanical factor promoting metal transfer.

Oscillation of the drop was caused by a combination of random acts of arc force oscillation and surface tension. Arc force could not detach the metal drop at one stroke, but accumulated the energy in the oscillation of the drop. At the moment when the surface tension was overcome by the superposition of arc force and inertial force, the drop was detached from the electrode.

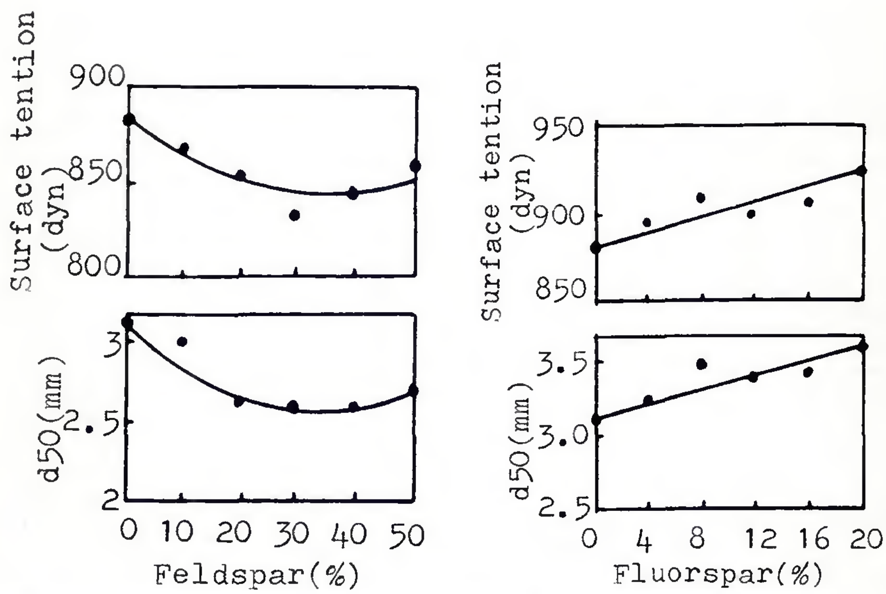

Fig. 16 — Relationship between d_{50} and surface tension and the composition of covering

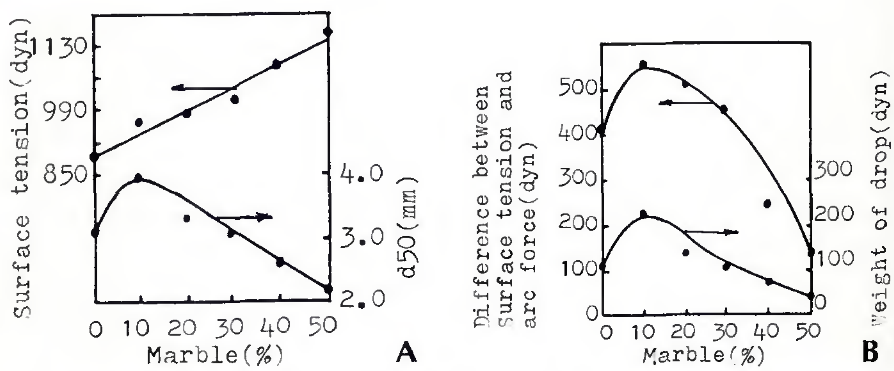

Fig. 17 — Relationship between: A — Surface tension and d_{50}; B — the force determined by subtracting the arc force from surface tension, and the weight of the drop of electrodes containing different marble contents

Estimation of the Equilibrium of Forces at the Moment of Detachment

The forces that acted on the molten drop at the tip of the stainless steel electrode with 30% marble in covering were estimated with the information below. From the data of the coefficient of the surface tension plotted in Fig. 7 and calculated by Equation 1, the force caused by surface tension at the temperature near the melting point was determined to be approximately 1000 dyn. By taking the overheating temperature of the drop at the time of detachment as being 300°C (572°F) higher than the melting point and the temperature coefficient of the surface tension as being 0.33 dyn/cm°C (Ref. 4), the force that opposed the transfer of the metal drop was estimated to be 900 dyn.

The arc force measured was 542 dyn, but only part of this pressure acted on the drop directly. By using the results presented in Fig. 10B, and noting that the increase in drop sizes resulting from increased baking temperature was caused by the decrease of arc force, and by comparing the changes of the arc force, drop weights and corresponding inertial force induced by oscillation, the effective coefficient of the acting arc force was estimated to be 0.57. The arc force that acted directly on the drop was estimated to be 309 dyn. The frequency and amplitude of the oscillation of the drop was measured as 25 Hz and 0.12 cm by x-ray high-speed photography. From the measured d_{50}, the statistical mass of the drops was calculated as 0.11 g. From this data and Equation 2, the inertial force induced by oscillation was estimated to be 326 dynes. The statistical weight of each drop was 108 dyn. The sum resultant of the forces that acted to detach the drop totaled 743 dyn, *i.e.*, with 15% error in the equilibrium of the surface tension. This equilibrium was acceptable.

Mechanism of Globular Transfer from Covered Electrodes

Based on the above measurements and quantitative and systematic analyses of the mechanical factors, a mechanism for globular metal transfer from covered electrodes was hypothesized. Arc force, which is produced by gas steam evolving mainly from decomposed carbonate and other components in the covering, acts on the melted metal drop at the tip of the electrode. Under the combined action of arc force and surface tension, the drop oscillates. As the drop grows, the effective arc force and the amplitude of oscillation increases. At the moment the downward force (i.e., the sum of arc force with the oscillatory inertial force and drop weight) exceeds the surface tension of the drop, it detaches from the electrode.

In Ref. 5, Lancaster summarized two mechanisms of metal transfer from covered electrodes proposed by Conrady and Becken. In Figs. 14 and 15, these two mechanisms are identified, but from the evaluation of a great many high-speed films, it was found that these two mechanisms operated only in exceptional cases for stainless steel and basic electrodes welded with DCEP polarity.

Conclusions

The results of an investigation of mechanical factors and the mechanism of globular metal transfer from covered stainless steel and basic electrodes operating with DCEP polarity are summarized as follows:

1) Surface tension is the main force that prevents the drop from transferring. When all other forces are held constant, the sizes of drops varied in proportion to surface tension.

2) Arc force is primarily produced by gases evolved from carbonates and other components, and is one of the main forces promoting metal transfer.

3) Inertial force induced by oscillation (*i.e.*, produced by a combination of arc force and surface tension) is one of the important forces promoting metal transfer.

4) In comparison with surface tension and arc force, the gravitational force of the drop is small, even with shielded metal arc welding.

5) The mechanism of globular metal transfer with stainless steel and basic covered electrodes is the following: the drop is detached from the tip of the electrode under the combined action of the drop weight, arc pressure and the inertial force induced by oscillation when it exceeds the force of the surface tension.

References

1. Conn, W. M. 1959. *Die Technishe Physik der Lichtbogen Schweissung.*
2. Lando, J. L., and Dakley, H. T. J. 1967. *Colloid and Interface Science.* Vol. 25, p. 526.
3. Ishizaki, K., *et al.* 1966. Symposium: *Physics of the Welding Arc,* London, England.
4. Pohodnia, N. K. 1972. *Gases in the Weld,* Moscow, U.S.S.R.
5. Lancaster, J. F. 1971. *Metal Construction,* Vol. 1, p. 370.

Corrosion Testing of Silver-Brazed Stainless Steel Joints in Tap Water

Chloride concentrations in tap water influenced the corrosion rates of two brazing filler metals but had little effect on another

BY H. -D. STEFFENS, B. WIELAGE AND W. BRANDL

ABSTRACT. Three different silver-based brazes (B-Ag 56 Cu-In-Ni, B-Ag 60 Cu-Sn and B-Ag 72 Cu) were investigated with respect to their corrosion behavior in tap water. As a result, it was found that the chloride concentration possesses a significant influence on the resistance of the joints produced with the filler metals B-Ag 56 In-Ni and B-Ag 60 Cu-Sn. While the former can be used in water up to 50 mg Cl^-/L without showing knife-line attack, the latter is feasible for higher chloride concentrations. For the braze B-Ag 72 Cu, it was determined that an increasing Cl^- content does not associate with a higher corrosion rate.

Introduction

The corrosion behavior of stainless steels and their brazed joints have been, and continue to be, the subject of numerous investigations.

Due to the heavy increase in water consumption and the accompanying increasing pollution of effluents, the corrosive aggressiveness of the waters carried in sanitary installations will increase over the next several years, at least in central Europe. The chemical aggressiveness of these media will, of course, vary widely, with pollution being heavy in densely populated industrial centers and less pronounced in predominantly agricultural and more thinly populated areas. From this follows the necessity to adapt materials more than is done today to these expected differences in corrosive attack and to consider the use, in certain areas, of materials with higher resistance to corrosion than the conventionally used plumbing materials, such as copper and galvanized steel. Particularly suitable are Cr-Ni-Mo steels which can be used in water with a chloride-ion content of up to 1000 mg/L.

Basically, three methods are suitable for joining Cr-Ni-Mo-steel pipe: welding, brazing and the use of press fittings with nonmetallic seals.

Joining of thin-walled stainless steel pipe by welding is a highly specialized joining technique which cannot be safely performed by a plumber at a construction site. Press fittings of passive stainless steel with nonmetallic seals are generally unsuitable due to crevice corrosion at contact areas between seal and steel pipe.

An alternative to press fittings is silver-brazing of stainless steel pipes. This is also suitable for joining nonferrous materials, such as copper, and can be done on-site. However, the often unfavorable corrosion behavior of brazed joints has so far argued against its practical use in house-plumbing applications. This paper summarizes the corrosion testing of silver brazed stainless steel joints in tap water.

KEY WORDS

Corrosion Testing
Silver-Brazed Joints
Tap Water Corrosion
Cr-Ni-Mo Pipe
Pipe Corrosion
Tap Water Piping
B-Ag 56 Cu-In-Ni 620-730
B-Ag 60 Cu-Sn 600-720
B-Ag 72 Cu 780 Alloy
Vacuum Furnace Braze

H. -D. STEFFENS, B. WIELAGE and W. BRANDL are with the University of Dortmund, Dortmund, West Germany.

Paper presented at the 17th International AWS Brazing Conference, held April 15–17, 1986, in Atlanta, Ga.

Experimental Materials

The material selected for the base metal was Cr-Ni-Mo-Ti 18-10 stainless steel. The brazing alloys used were B-Ag 56 Cu-In-Ni (620-730), B-Ag 60 Cu-Sn (600-720) and B-Ag 72 Cu (780)—Table 1.

Table 1—Chemical Composition of Brazing Alloys

Brazing Alloy	Chemical Composition % Ag	Cu	Sn	Ni	In
B-Ag 56 Cu-In-Ni (620-730)	56	26	—	4	14
B-Ag 60 Cu-Sn (600-720)	60	30	10	—	—
B-Ag 72 Cu (780)	72	28	—	—	—

Production of Brazed Joints

For the production of brazed joints, seamless cold-drawn pipe with an internal diameter of 15 mm (0.6 in.) and a wall thickness of 1.5 mm (0.06 in.) was used, brazing being done with braze fittings. The braze filler metal was available in wire form (thickness 1.2 mm/0.05 in.). Rings were made from the wire for brazing. Brazing was done with a fluxing agent in air for the first two brazes mentioned and in a vacuum furnace for the third. The joint clearance for the furnace braze was set at 0.05 mm, and for brazing in air, a joint clearance of 0.1 mm was used.

The structure of the brazed joint produced with Braze B-Ag 56 Cu-In-Ni 620-730 is shown in Fig. 1.

It is composed of three phases. The copper-rich α-phase in the brazed joint is visible in the form of large-area, dark regions and occurs at the base-to-braze interface as a coherently precipitated phase. The matrix consists of silver-rich α_1 phase (large, light-colored regions in Fig. 1). The finely precipitated phase in the matrix is the Ag-In β_1 phase.

Figure 2 shows the structure of Braze B-Ag 60 Cu-Sn 600-720 after brazing. It also consists of three phases, the silver-rich matrix (light colored α_1 phase), a β phase (containing Ag and Sn) finely precipitated in the matrix, and the copper-rich α phase. In contrast to Braze B-Ag 56 Cu-In-Ni, however, the α-phase has not been precipitated as a coherent seam at

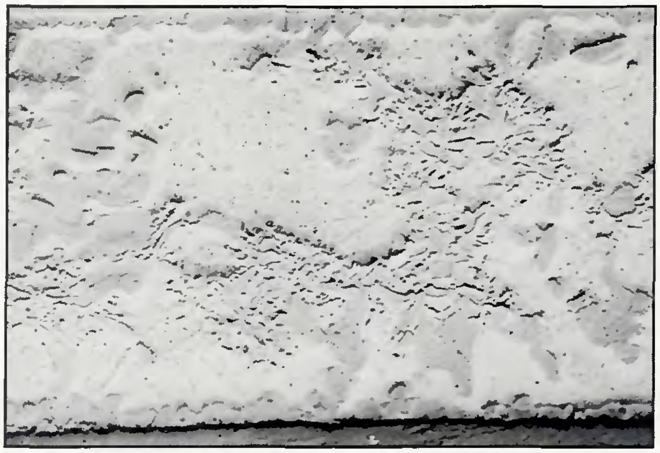

Fig. 1 — Cr-Ni-Mo-Ti 18-10 stainless steel/B-Ag 56 Cu-In-Ni 620-730 brazed joint

Fig. 2 — Cr-Ni-Mo-Ti 18-10 stainless steel/B-Ag 60 Cu-Sn 600-720 brazed joint

Fig. 3 — Cr-Ni-Mo-Ti 18-10 stainless steel/B-Ag 72 Cu 780 brazed joint,

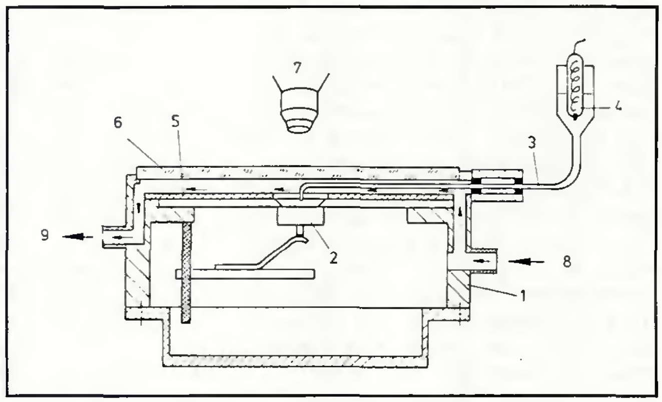

Fig. 4 — Corrosion testing device. (1) work cell; (2) the specimen; (3) salt bridge probe; (4) reference electrode; (5) auxiliary electrode; (6) Plexiglas plane; (7) stereomicroscope; (8 and 9) the electrolyte flow path

the braze-to-base interface.

The eutectic structure of the silver-braze B-Ag 72 Cu 780 is shown in Fig. 3.

Methods of Investigation

To investigate the corrosion behavior of the brazed joint in Dortmund drinking water (Table 2), electrochemical tests were made. The influence of the chloride content of the water on the polarization behavior of the brazed joints was investigated. Chloride contents were varied from 25 to 500 mg/L.

In order to reproduce the conditions existing in pipelines in regard to oxygen content and flow patterns, an experimental device was used in which fresh water flowed over the specimen at a constant rate — Fig. 4.

Table 2—Analysis of Dortmund Tap Water

Total hardness GH	8.70	°dH
Carbonate hardness KH	5.90	°dH
pH value	7.76	
Electrical conductivity	381.00	μS/cm
Cl^- content	38.80	mg/L
CO_2 content	2.00	mg/L
O_2 content	6.40	mg/L
Temperature condition	15.00	°C

Corrosion Testing Device

The work cell of the corrosion testing device is made of polyvinylchloride. A contact pin is provided whereby the specimen is connected to the work electrode via the anode rod. The auxiliary electrode is arranged in a circle around the work electrode. Potential measurement was made via the salt bridge probe with the aid of the reference electrode. For all measurements, a saturated calomel electrode was used as the reference electrode. Observation of the specimen during the test was made possible through the Plexiglas pane by means of a stereomicroscope. The electrolyte flowed through the work cell from end to end and the probe was positioned in the direction of flow. The rate of flow was variable.

The continuous, metered addition of sodium chloride solution required for variation of the chloride content was achieved with the aid of a micropump. Prior to the test, the specimens were ground and polished with diamond paste to a 1 μm finish.

Test Results

Experimental Results in Tap Water

The current density versus potential curves of the base metal Cr-Ni-Mo-Ti 18-10 stainless steel brazed with the three different silver brazes in tap water with a chloride content of 25 mg/L are shown in Figs. 5-7. For the purposes of comparison, the current density versus potential curve of the base material is also shown in these figures. The steady-state potentials of the brazed joints are, without exception, more positive than those of the base material. Appearance of the braze joint in its initial state at potential P_1 alters during the polarization test at different potentials referred to as P_2, P_3, P_4 and P_5.

Figure 8 shows the change in the structure of the braze joint during the polarization test carried out on the Cr-

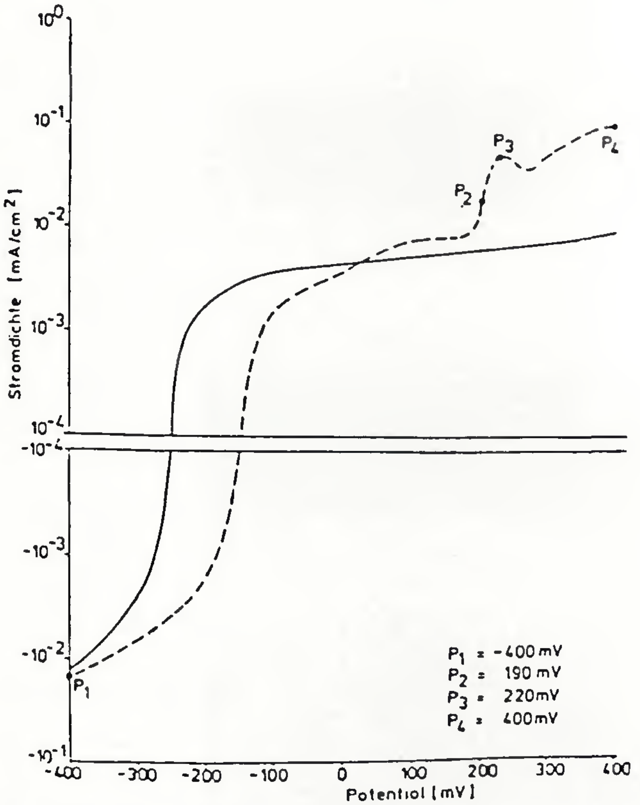

Fig. 5—Polarization curve of Cr-Ni-Mo-Ti 18-10 stainless steel/B-Ag 56 Cu-In-Ni joint in tap water

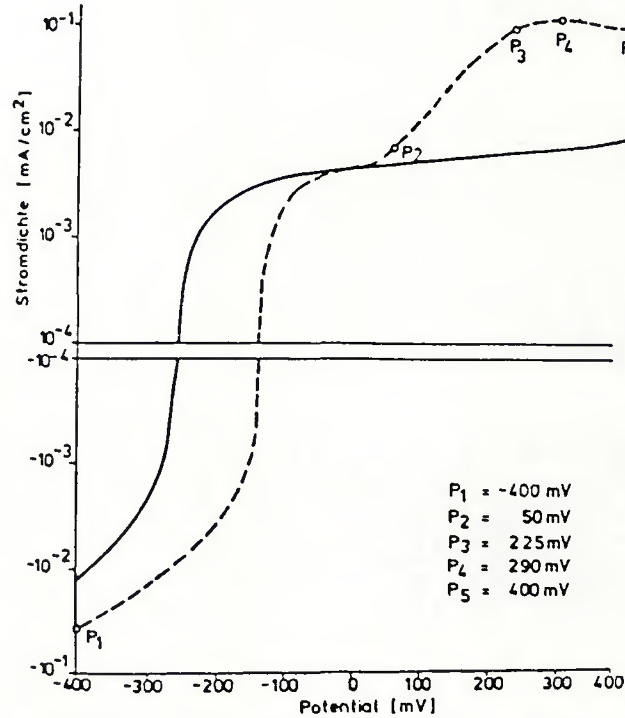

Fig. 6—Polarization curve of Cr-Ni-Mo-Ti 18-10 stainless steel/B-Ag 60 Cu-Sn joint in Dortmund tap water

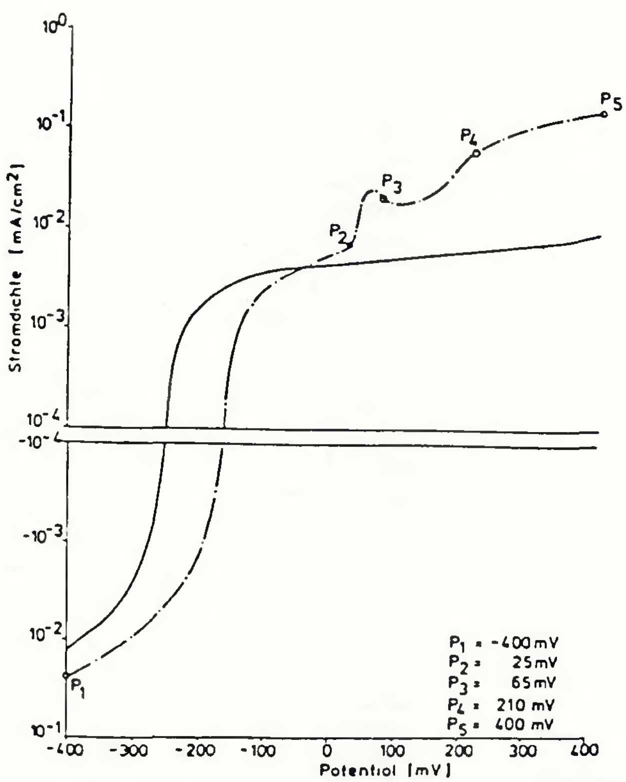

Fig. 7—Polarization curve of Cr-Ni-Mo-Ti 18-10 stainless steel/B-Ag 72 Cu joint in Dortmund tap water

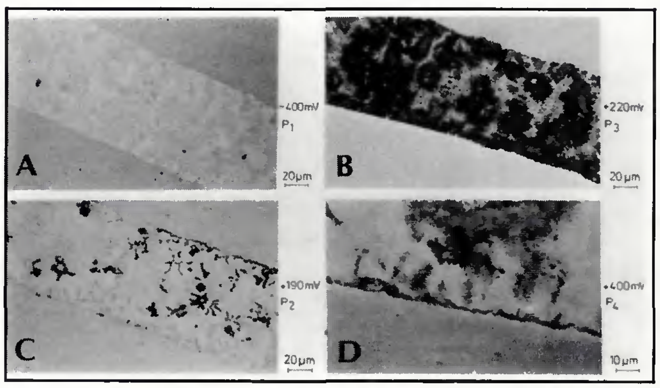

Fig. 8—Appearance of B-Ag 56 Cu-In-Ni brazed joint during electrochemical polarization. A—Initial structure at −400 mV; B—corrosive attack begins, +190 mV; C—brownish layer forms, +260 mV; D—corrosion grows into a dense, firmly adhering layer, +400 mV

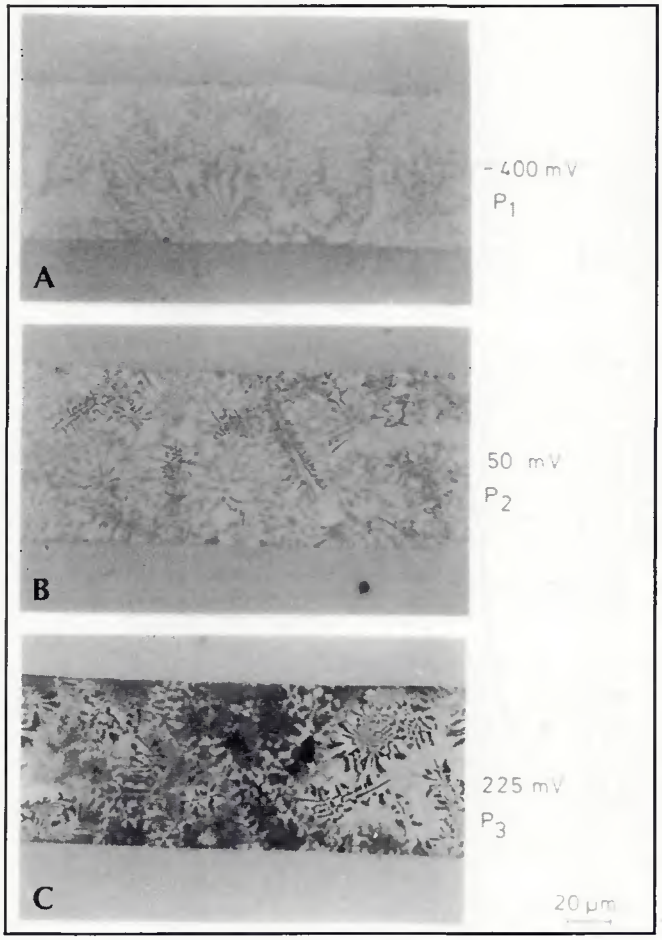

Fig. 9 — Appearance of B-Ag 60 Cu-Sn brazed joint during polarization. A — Original structure; B — initial corrosive attack; C — corrosion intensifies

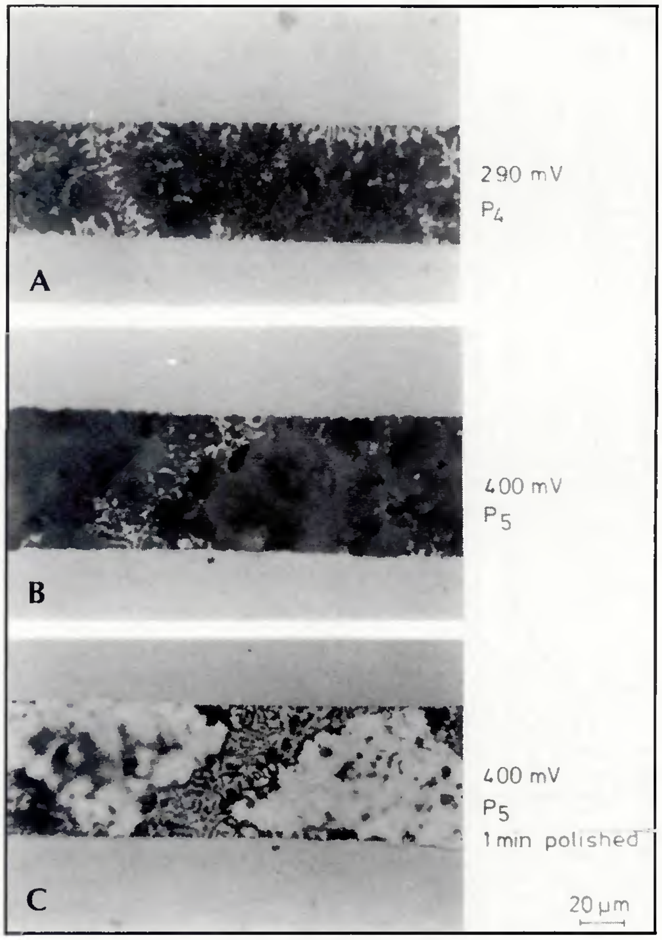

Fig. 10 — Appearance of B-Ag 60 Cu-Sn brazed joint during polarization. A — Formation of second layer begins; B — growths continue; C — strong adhesion of layer, even after one minute of polishing

Ni-Mo-Ti 18-10 stainless steel/B-Ag 56 Cu-In-Ni brazed joint.

The initial structure of the brazed joint (Fig. 8A) at −400 mV (Point P_1 on the current density versus potential curve — Fig. 5) begins to change from about +190 mV (Point P_2), onward. There are indications of corrosive attack on the α-Cu phase in the joint and at the braze-to-base interface — Fig. 8B. This incipient corrosion grows as the anodic polarization increases, which is associated with a steep rise in current density — Fig. 5.

With the fall of the current density at P_3 (Fig. 5) a brownish layer begins to form (Fig. 8C), with the formation completed at about +260 mV; the formation of this layer starts from the α-Cu phase. The renewed rise in current density from 260 mV onward (Fig. 5) is associated with an attack on the silver matrix (α_1-Ag-rich phase). As the α_1-Ag phase goes into solution, however, a dense, firmly adhering layer grows in these areas of the brazed joint — Fig. 8D.

The appearance of the Cr-Ni-Mo-Ti 18-10 stainless steel/B-Ag 60 Cu-Sn brazed joint during the polarization test is shown in Figs. 9 and 10.

The original structure of the braze (Fig. 9A, Point P_1) changes from about 50 mV onward (Point P_2 in Fig. 6). The α-Cu phase sustains the initial corrosive attack — Fig. 9B. With increasing polarization, up to about 225 mV (Point P_3), there is a massive rise in current density. The incipient corrosion of the copper-rich phase intensifies and a layer begins to form from the α-Cu phase — Fig. 9C. At the highest current density of the polarization curve (at about 290 mV, P_4 in Fig. 6) the formation of a second layer begins — Fig. 10A. This layer covered the entire brazed joint at increasing polarization and exhibited no tendency to be flushed off — Fig. 10B. Figure 10C illustrates the strong adhesion of this layer after a minute's polishing; a light-colored covering layer (top layer) was formed, which had grown beyond the edge of the brazed joint. In contrast to Braze B-Ag 56 Cu-In-Ni, only minor corrosive attack was detected on the remaining structure.

In polarizing the Cr-Ni-Mo-Ti 18-10 stainless steel/B-Ag 72 Cu-brazed joint, some initial corrosive attack was noted at +25 mV (Point P_2 in Fig. 7). The appearance of the brazed joint at +25 mV is shown in Fig. 11A.

In the eutectic structure, the copper-rich solid solution is preferentially attacked. In the further stages of the current density versus potential curve, the current density drops. This drop is accompanied by the formation of a layer. The renewed steady rise in current density, which points to increased dissolution of the silver-rich phase, subsequently levels off slightly at about 210 mV. It is here that a further layer begins to form starting at the edge of the brazed joint (Fig. 11B) completely covering the brazed joint at 400 mV. Extended polishing proved incapable of removing this layer, indicating how firmly adhered it was.

In summarizing the test results of the Dortmund tap water, one can state that under these conditions of water composition and temperature, *i.e.*, room temperature (Table 2), all three brazes exhibited good stability, with Braze B-Ag 72 Cu performing best. With this particular braze, the depth of attack was the lowest, while the top layer, which forms in the process, adheres firmly. No corrosive attack was noted on the base metal. While Braze B-Ag 56 Cu-In-Ni with the copper-rich α-phase does sustain some

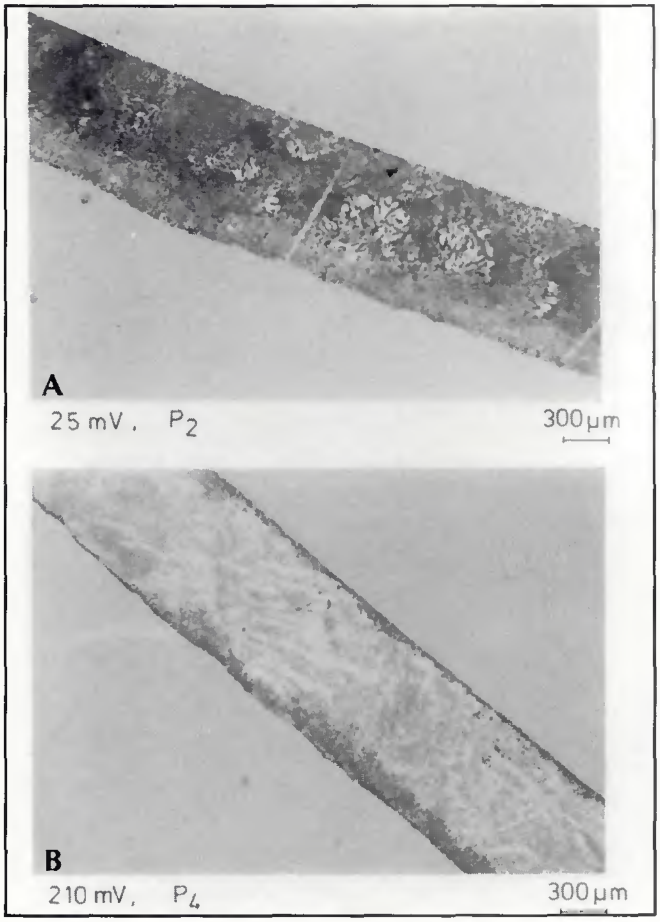

Fig. 11 — Appearance of B-Ag 72 Cu brazed joint during polarization. A — initial corrosive attack; B — second layer forms at edges of joint

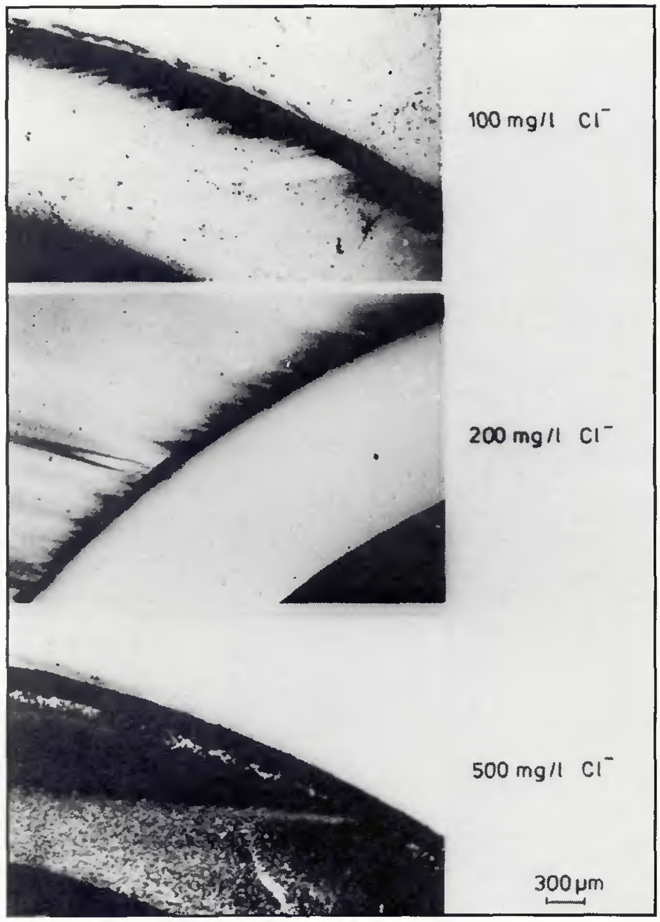

Fig. 12 — Appearance of B-Ag 56 Cu-In-Ni brazed joint after polarization in tap water

corrosive attack, no knife-line attack was observed at the chloride ion concentrations used in this work.

Experimental Results in Tap Water with Different Chloride Contents

With the stepwise increase of the chloride content, Braze B-Ag 56 Cu-In-Ni showed increased corrosive attack in the brazed joint (Fig. 12) and knife-line attack for chloride ion concentrations from about 50 mg/L or higher.

Figure 13 shows the current density versus potential curve for this brazed joint at chloride concentrations in Dortmund tap water of 25, 100, 200 and 500 mg/L.

The curves hardly differ from one another up to chloride contents of 200 mg/L. However, the appearance of corrosion at the brazed joint is very diverse — Figs. 8D and 14.

At 25 mg/L chloride, no knife-line attack could be detected at the braze-to-base interface (Fig. 8D), and at 100 mg/L chloride, the interface has been partly dissolved, while at 200 mg/L chloride, it is completely dissolved — Fig. 14. This phenomenon is even more pronounced at the maximum chloride con-

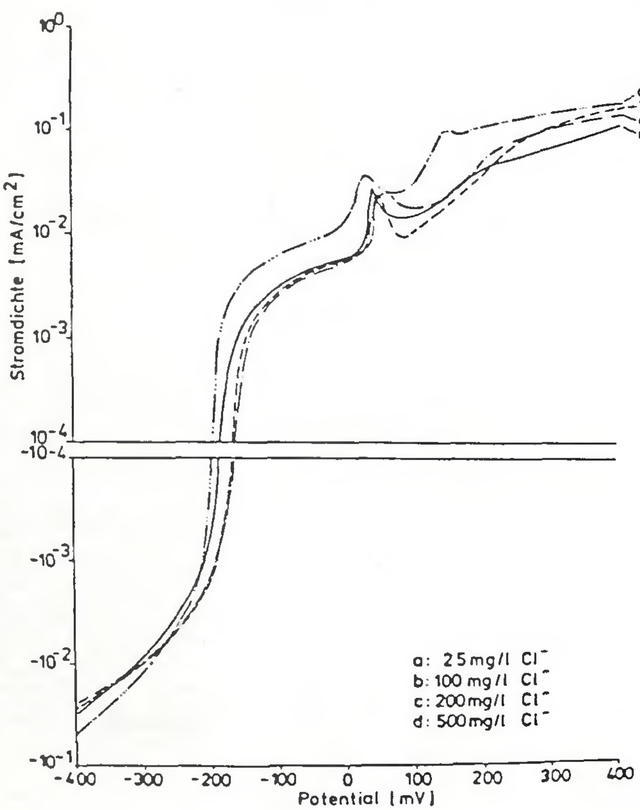

Fig. 13 — Polarization curves of Cr-Ni-Mo-Ti 18-10 stainless steel/B-Ag 56 Cu-In-Ni brazed joints

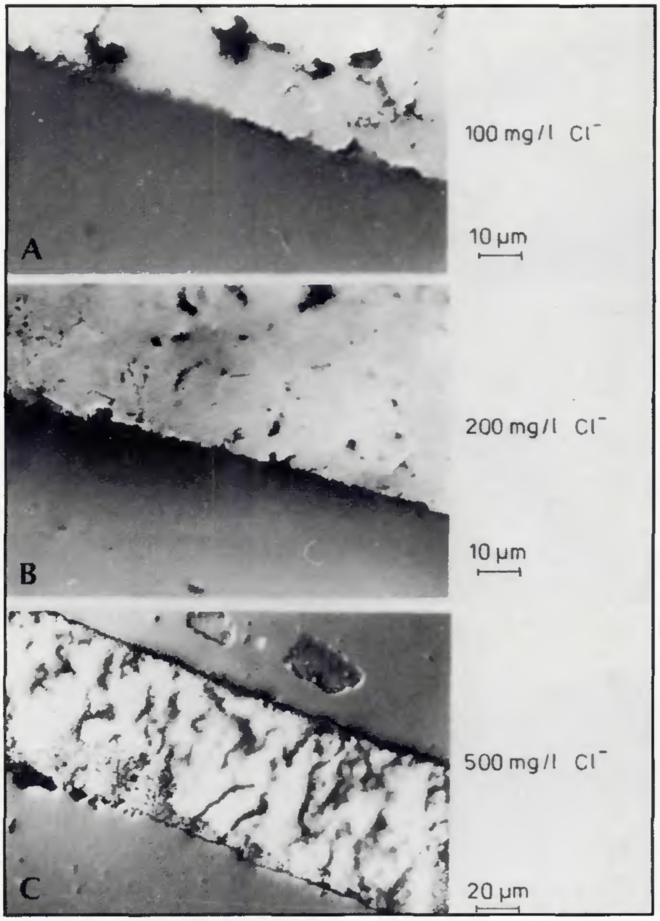

Fig. 14 — B-Ag 56 Cu-In-Ni after polarization in tap water

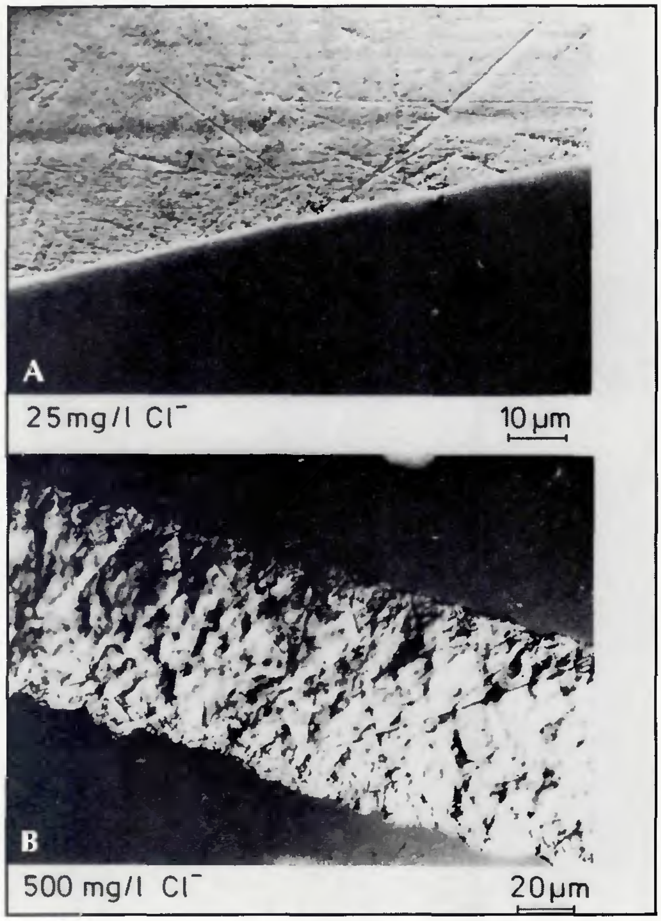

Fig. 15 — Surface layers formed on B-Ag 72 Cu joints in tap water

tent of 500 mg/L — Fig. 14. For these chloride concentrations, the current densities are, by comparison, considerably higher — Fig. 13.

The corrosive attack of Cr-Ni-Mo-Ti 18-10 stainless steel/B-Ag 60 Cu-Sn-brazed joints increased with increasing chloride content, too. The attack on the α phase, as well as the associated layer formation, undergo a shift towards more negative potentials. The same also applies to the corrosive attack on the silver-rich phase and the layer formation proceeding from it. Nevertheless, no preferential attack could be detected at the braze-to-base interface.

With the joint made with brazing alloy B-Ag 72, a phenomenon was found, as yet unexplained. At low (25 mg/L) and high (500 mg/L) chloride contents, firmly adhering layers form, which completely cover brazed joint. Yet, after polishing, they vary in appearance, suggesting differences in composition — Fig. 15.

At intermediate chloride contents (100 and 200 mg/L), only incomplete coverage of the brazed joint occurs (Figs. 16B and C), with the structure having been attacked only slightly.

Clarification of these phenomena, possibly attributable to the influence of chloride content on carbonate equilibrium, is the subject of further work.

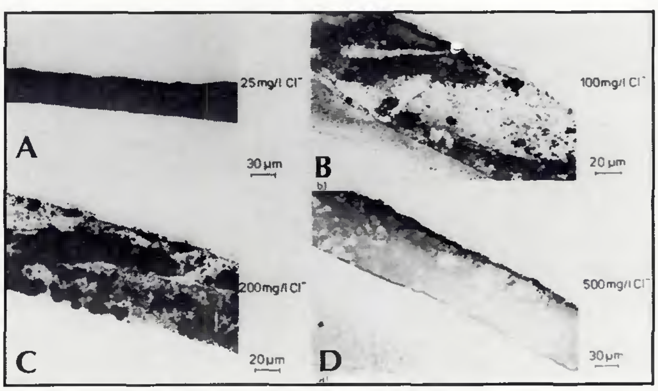

Fig. 16 — Appearance of B-Ag 72 Cu brazed joints after polarization in tap water with different chloride contents. A — Corrosion completely covers the joint; B — incomplete coverage; C — coverage grows; D — layer firmly adheres across the joint

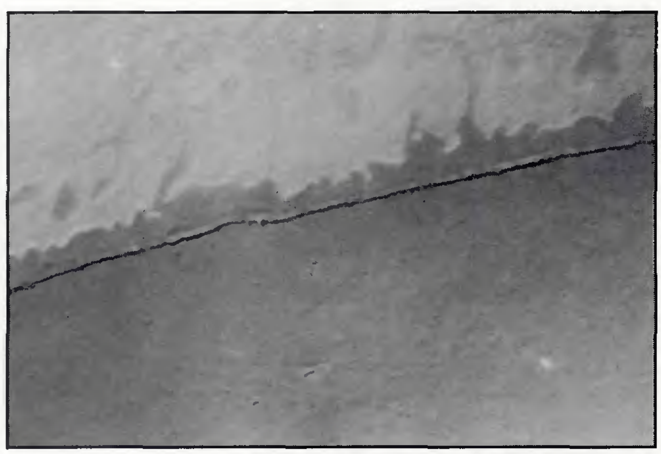

Fig. 17 — B-Ag 56 Cu-In-Ni brazed joint

Conclusion

The Braze B-Ag 56 Cu-In-Ni can be used in cold drinking water up to approximately 50 mg of chloride per litre. At higher chloride contents, increasing susceptibility of knife-line attack must be expected. According to present findings, this susceptibility is not due to the constant precipitation of the less noble α phase at the brazed joint, but rather to a very thinly formed intermediate layer, which still requires exact identification—Fig. 17. The preferred attack of this intermediate layer probably leads to the failure of the joint.

While the joint made with the Braze B-Ag 60 Cu-Sn is subject to stronger attack at rising chloride contents, no preferred attack at the base-to-braze phase boundary takes place. Hence this braze, on the basis of the electrochemical tests, can also be used in drinking water with higher chloride contents.

The test results obtained on the joints made with the Braze B-Ag 72 Cu indicate that an increasing chloride content of the electrolyte, *e.g.*, tap water, is not necessarily associated with a higher rate of corrosion. The variations in the formation of the covering layer that were found here, are to be clarified in further research work by correlating electrochemical tests and the results of plant corrosion tests with surface-analytical measuring techniques, especially Auger Electron Spectroscopy. Since this method also allows the composition of the layer with depth to be determined (by incremental removal of material by argon sputtering), inferences as to the formation mechanisms of the covering layers with regard to the polarization potential and water composition may be deduced.

RESEARCH/DEVELOPMENT/RESEARCH/DEVELOPMENT/RESEARCH/DEVELOPMENT/RESEARCH/DEVELOPMENT/RESEARCH/DEVELOPMENT

Significant Features of High-Strength Steel Weld Metal Microstructures

Optimal combinations of microstructure and mechanical properties are identified for high-strength steel submerged arc weld metal

BY P. T. OLDLAND, C. W. RAMSAY, D. K. MATLOCK AND D. L. OLSON

ABSTRACT. Microstructural changes with heat input during submerged arc welding of a high-strength, low-carbon, 5 wt-% nickel Cr-Mo steel were evaluated with both optical and transmission electron microscopy (TEM), and the results were correlated with mechanical properties. A classification scheme was developed to identify the complex microstructural features observed in the TEM analysis of high-strength steel weld metal. An increase in heat input from 1 to 4 MJ/m (25 to 100 kJ/in.), decreased the strength, increased the ductility and the toughness, and caused the weld metal microstructure to change from autotempered martensite to a mixture of martensite, bainite, and retained austenite. An optimal combination of microstructure and properties was identified, and the potential for modifying the consumable compositions to produce this structure over a wide range of heat inputs was discussed, based on continuous cooling transformation behavior.

Introduction

The economical utilization of high-strength steels with yield strengths greater than 690 MPa (100 ksi) in fabricated structures depends on the use of high-heat-input welding processes, proper selection of welding consumables, and preheat and postweld heat treatment procedures. Significant literature on the welding of high-strength steel exists, but much of this work is focused on the heat-affected zone microstructure and properties (Refs. 1-6). There is only limited literature on the microstructure and properties of high-strength-steel weld metal (Refs. 7-10).

P. T. OLDLAND, C. W. RAMSAY, D. K. MATLOCK and D. L. OLSON are with the Center for Welding Research, Colorado School of Mines, Golden, Colo.

Paper presented at the 69th Annual AWS Meeting, held April 17-22, 1988, in New Orleans, La.

The submerged arc welding process has been successfully applied (Ref. 11) to lower-strength "ferritic" steels with yield strengths less than 690 MPa in the 1 to 4 MJ/m (25 to 100 kJ/in.) heat input range. In contrast, submerged arc welding of high-strength steels with heat inputs greater than 2 MJ/m (50 kJ/in.) does not yet consistently produce weldments with acceptable combinations of strength and toughness (Ref. 11). To extend the usable heat input ranges for submerged arc welding of high-strength steels, a quantitative characterization of the microstructure and mechanical properties is required. A fundamental understanding of the influence of heat input on the microstructure and properties of high-strength-steel weld metal will lead to increased utilization of these materials.

Variations in high-strength-steel weld metal microstructures and properties are primarily due to two factors: the cooling rate and the weld metal composition. The cooling rate experienced by the weld metal deposit is controlled by a combination of heat input and heat extraction. The heat extraction from the weld pool depends on joint geometry, plate thickness, and extent of preheat. The rate of heat extraction increases with an increase in plate thickness or a decrease in the preheat temperature. The weld metal composition is dependent on base metal and electrode wire compositions, dilution, and the pyrometallurgical chemical reactions in the welding arc. The final microstructures in steel weld deposits result from austenitic decomposition, either through the nucleation and growth of ferrite and bainite or through the athermal transformation to martensite, which can be modified by a variety of precipitation reactions (Ref. 12). Previous studies have shown that weld metals with yield strengths less than 560 MPa (80 ksi) consist primarily of ferrite, while weld metals with yield strengths greater than 690 MPa (100 ksi) consist primarily of martensite and bainite (Refs. 13-15). In this paper, a detailed analysis of effects of heat input on microstructural development in high-strength-steel weld metal is presented.

KEY WORDS

High-Strength Steel
HY-130 Steel Welds
Weld Microstructures
Submerged Arc Welding
Emission Spectrometer
ARL Spectrometer
Optical Metallography
Martensite + Bainite
Fractography

Experimental Procedure

A low-carbon, 5 wt-% nickel Cr-Mo high-strength steel was received in the form of 51-mm (2-in.) thick plate, and welds were prepared with two welding wires, identified as wire 1 and wire 2, and one commercial basic welding flux. Complete chemical analyses of the base metal and welding wires are presented in Table 1. The nominal composition of the flux used in this study is listed in Table 2. Single-pass, bead-on-plate weldments were prepared by the submerged arc welding process over a heat input range of 1.2 to 3.7 MJ/m (30 to 93 kJ/in.) for five test series. Series I and II weldments were produced on 300- × 51- × 19-mm (12- × 2- × 0.75-in.) coupons using electrode wires 1 and 2. These initial weldments were used in a screening process to determine the compositional stability, hardness, and microstructural changes occurring with changes in heat input. Series III weldments, which were used for the majority of this study, were produced on 690- × 76- × 51-mm (27- × 3- × 2-in.) coupons with a 6.5-mm-deep (0.25-in.) 60-deg included angle groove, using electrode wire 1. The larger coupons were used to provide a significant heat sink. However, the cooling rate in the laboratory coupons may be less than would be obtained in full-size structures.

Table 1—Chemical Compositions of the 5 wt-% Nickel Cr-Mo High-Strength-Steel Base Metal, Welding Wires and Flux

Material	C	Mn	Si	P	S	Ni	Mo	Cr	Cu	V	Ti
Base plate	0.09	0.72	0.28	0.007	0.003	4.85	0.41	0.55	0.15	0.080	0.005
Wire 1	0.076	1.55	0.39	0.004	0.002	2.47	0.80	0.73	0.031	0.003	0.016
Wire 2	0.093	1.71	0.24	0.006	0.004	2.10	0.63	1.02	0.047	0.010	0.010

Table 2—Nominal Chemical Composition of Submerged Arc Welding Flux in wt-%

	SiO_2	Al_2O_3	MgO	MnO	CaO	TiO_2	CaF_2	Na_2O	Fe_2O_3	C
Flux	10.7	17.2	31.7	6.6	1.1	0.86	24.1	0.78	1.9	0:35

The weld groove was necessary to provide enough weld bead for mechanical testing and to yield approximately the same dilutions obtained in Series I and II weldments. Additional weld metal produced in Series III was used for Series IV and V in an attempt to simulate the effects of reheating of weld metal during multipass welding. This was accomplished by heat treating two sets of Charpy V-notch samples for 1 min at 688° and 832°C (1270° and 1529°F), for Series IV and V, respectively, followed by air cooling. Diamond pyramid hardness measurements were made on the tempered weld metal and the Series III weld metal for comparison. These tempered specimens were broken at temperatures near the ductile-to-brittle transition temperatures of the untempered welds.

Chemical analyses of the as-received base plate and the weld metal of Series I, II, III, IV and V were obtained using an ARL emission spectrometer (for the elements manganese, silicon, phosphorus, nickel, molybdenum, chromium, copper, vanadium and titanium) and with a Leco interstitial combustion analyzer (for carbon and sulfur).

Weldments produced in Series I, II and III were evaluated with standard optical metallographic methods to characterize both the macrostructure and microstructure of each weld. The weld metal specimens were sectioned transverse to the welding direction, mounted, and mechanically polished through 0.05 μm Al_2O_3 powder. Several special etchants were used in this study, and it was determined that LePera's etch (Ref. 16) revealed details of the solidification structure that were not observable with standard Nital steel etchants. The LePera's and Nital etchants, the etching procedure, and their effect on the microstructure are presented in Table 3. The samples were etched with LePera's etch, analyzed, repolished, etched with Nital, and analyzed again. Longitudinal sections were prepared in the Series III weldments near the centerline to obtain, along with the transverse micrographs, a three-dimensional view of the weld metal microstructures. Series III specimens used for optical microscopy were analyzed using a scanning electron microscope with energy dispersive x-ray spectrometry. Series III weld metal specimens, which were analyzed with the transmission electron microscope, were punched from wafers of weld metal cut transverse to the welding direction. These wafers were polished with a twin-jet electropolisher in 5 vol-% perchloric acid, and 95 vol-% acetic acid solution at 13°C (55°F).

Hardness measurements were made on the transverse sections of Series I, II and III welds using the Rockwell hardness tester. Mechanical testing of the Series III welds consisted of tensile testing of flat all-weld-metal tensile bars in accordance with ASTM standards (Ref. 17), with a reduced gage section of 25 × 6.3 × 3.7 mm (1 × 0.25 × 0.14 in.), and Charpy V-notch toughness testing. ASTM standard 5-mm-thick (0.2-in.) subsized Charpy specimens (Ref. 18) were machined from Series III, IV and V welds. The notches were oriented to cause crack propagation along the weld centerline in the welding direction.

Fracture surfaces of Series III Charpy V-notch samples broken at −196°C (−321°F) were analyzed using energy dispersive x-ray spectrometry on the scanning electron microscope. The features of the fracture surfaces were then compared to the weld metal microstructures. A qualitative analysis of some inclusions present on the fracture surfaces was conducted during this study.

Results

Compositional Stability

The weld metal chemical compositions and delta quantities for Series I, II and III are listed in Table 4. The data in Table 4 include the series number, heat input, and dilution for each weld specimen as calculated directly from measurements of bead geometry. Here, the dilution was held to a range of 45 to 55%.

The compositional stability of the weld deposit was evaluated using the delta quantity (Ref. 19). The delta quantity is the difference between the analytical (measured) weld metal composition and the predicted (calculated) weld metal composition, based on dilution of the electrode wire and the melted base metal. The delta quantity directly reflects the chemical reactions occurring during welding. A positive delta quantity for an element indicates that the element was added to the weld pool from the flux. A

Table 3—Summary of Special Etchants, Etching Procedure and the Etching Effect on the Weld Metal Microstructure

Etchant	Procedure	Effect on Microstructure
Nital	2% nitric in methanol. Swab at room temperature for approximately 45 seconds.	Etches grain boundaries. Highlights second phase, such as martensite, and bainite.
LePera's	1% sodium metabisulfate in distilled water plus 4% picric acid in ethanol, mixed in a 1:1 volume ratio. The specimen should be etch-polished using 4% picral to remove all the disturbed metal (approximately three etch-polished sequences are sufficient). The etchant is then mixed and the specimen is immediately immersed for 5-10 seconds.	Martensite appears white, bainite appears black, ferrite appears tan (or gray). Shows coring of solidification structure in weld metal.

Table 4—Chemical Compositions, Delta Quantities, Heat Inputs and Dilutions for Series I, II and III, Single-Pass Weld Metal, in wt-%

Series Number	Heat Input MJ/m	Dilution	Compositions										
			C	Mn	Si	P	S	Ni	Mo	Cr	Cu	V	Ti
I	1.1	0.51	0.090	1.20	0.35	0.012	0.004	3.27	0.52	0.82	0.08	0.044	0.008
	2.6	0.52	0.084	1.29	0.37	0.012	0.003	3.29	0.54	0.85	0.09	0.044	0.008
	3.6	0.43	0.078	1.32	0.38	0.013	0.005	3.21	0.55	0.89	0.07	0.041	0.008
II	1.1	0.56	0.082	1.19	0.41	0.011	0.003	3.64	0.64	0.71	0.09	0.042	0.009
	1.6	0.51	0.078	1.18	0.41	0.011	0.002	3.56	0.65	0.66	0.08	0.042	0.010
	1.8	0.53	0.083	1.14	0.38	0.010	0.003	3.42	0.62	0.66	0.08	0.042	0.009
	2.6	0.49	0.078	1.18	0.40	0.011	0.004	3.55	0.65	0.66	0.07	0.041	0.009
	2.8	0.47	0.073	1.19	0.41	0.012	0.002	3.30	0.65	0.68	0.07	0.038	0.009
	3.7	0.43	0.075	1.23	0.41	0.012	0.002	3.46	0.66	0.69	0.07	0.039	0.010
III	1.2	0.55	0.087	1.23	0.35	0.012	0.004	3.20	0.49	0.83	0.08	0.040	0.009
	2.5	0.50	0.076	1.23	0.38	0.013	0.003	3.20	0.50	0.84	0.08	0.040	0.009
	3.7	0.44	0.077	1.24	0.38	0.014	0.004	3.20	0.49	0.85	0.08	0.040	0.009

Series Number	Heat Input MJ/m	Dilution	Delta Quantities										
			C	Mn	Si	P	S	Ni	Mo	Cr	Cu	V	Ti
I	1.1	0.51	−0.002	−0.01	0.09	0.005	0.000	−0.23	0.00	0.03	−0.21	−0.001	0.000
	2.6	0.52	−0.007	0.10	0.11	0.005	0.000	−0.25	0.02	0.08	−0.02	0.002	−0.001
	3.6	0.43	−0.013	0.04	0.12	0.007	0.000	−0.08	0.01	0.07	−0.02	0.002	0.000
II	1.1	0.56	−0.002	0.06	0.07	0.004	0.000	0.00	0.00	0.07	0.00	0.000	−0.002
	1.6	0.51	−0.004	0.05	0.08	0.005	−0.001	−0.11	0.05	0.02	−0.01	0.000	0.002
	1.8	0.53	0.000	0.03	0.05	0.004	0.000	−0.31	0.02	0.02	−0.02	−0.002	−0.001
	2.6	0.49	−0.004	0.03	0.07	0.005	0.000	−0.13	0.03	0.04	−0.02	0.001	−0.002
	2.8	0.47	−0.010	0.05	0.07	0.007	0.001	−0.28	0.03	0.03	−0.02	−0.001	−0.002
	3.7	0.43	−0.006	0.07	0.06	0.007	0.000	−0.03	0.03	0.03	−0.01	0.003	−0.001
III	1.2	0.55	−0.004	0.07	0.10	0.005	0.004	−0.26	−0.01	0.07	−0.011	−0.006	0.001
	2.5	0.50	−0.015	0.02	0.13	0.006	0.004	−0.13	−0.02	0.06	−0.007	−0.003	0.001
	3.7	0.44	−0.015	−0.03	0.13	0.007	0.003	0.00	−0.04	0.04	−0.003	0.001	0.001

negative delta quantity for an element indicates that the element was extracted from the weld pool due to chemical reactions with the liquid flux. The elements that exhibited significant delta quantities were carbon, manganese and silicon. The delta quantities for these three elements were shown to be independent of heat input in the 1 to 4 MJ/m range. Silicon and manganese had positive delta quantities of 0.10 wt-% and 0.05 wt-%, respectively. However, the compositional changes to the weld pool represented by these delta quantities do not have a significant effect on the hardenability of the weld metal (Ref. 20). Carbon had a negative delta quantity, resulting in a decrease in the weld metal carbon content of approximately 0.01 wt-% to a mean value of 0.081 wt-%. As shown in Table 4, the delta quantities for the remaining alloying elements were negligible.

In general, the weld metal composition was stable with a change in heat input. This stability results primarily from the use of a highly basic flux with a low silica content. Silica is a major oxygen source in submerged arc welding, and thus the low silica content minimizes the oxidation potential of the weld pool (Ref. 21). The delta quantities remained constant with variations in heat input. This observation suggests that variations in wire composition can be conveniently used to make systematic alterations of the weld metal composition and, thus, weld microstructure and properties. This also suggests that variations in cooling rate with changes in heat input are responsible for the observed microstructural changes discussed below.

Mechanical Properties

The mechanical properties of the weldments varied systematically with heat input. The hardnesses of the weld metal produced in Series I and II on 300- × 51- × 19-mm coupons, and Series III on 690- × 76- × 51-mm coupons are shown in Fig. 1. For all three series, the hardness decreased with an increase in heat input. The hardness of Series I weld metal produced with wire 1 decreased from Rockwell C 38 at 1.2 MJ/m (31 kJ/in.) to Rockwell C 31 at 3.7 MJ/m (94 kJ/in.). The hardness of the Series II weld metal produced with wire 2 was consistently lower than that of Series I weld metal, and varied from Rockwell C 37 at 1.2 MJ/m to Rockwell C 29 at 3.7 MJ/m. The thicker plate and the more complex geometry used for Series III resulted in higher cooling rates at a given heat input. Therefore, the Series III weld metal hardnesses produced with wire 1 were consistently higher than the corresponding data for Series I and II weld metal, and varied from Rockwell C 39 at 1.2 MJ/m to Rockwell C 35 at 3.7 MJ/m.

Figure 2 shows the room-temperature tensile properties of Series III weld metal as a function of heat input. Both the yield and ultimate tensile strengths decreased and the elongation to failure increased with an increase in heat input. As shown in Fig. 2, an increase in the heat input by a factor of three results in a decrease in the yield strength from 950 MPa (140 ksi) to 850 MPa (120 ksi), a decrease in ultimate tensile strength from 1240 MPa (180 ksi) to 1080 MPa (160 ksi), and an increase in the tensile ductility from 10 to 15%. The data in Fig. 2 correspond directly to the hardness data in Fig. 1.

Energy absorbed and percent brittle fracture versus test temperature transition curves were obtained for ASTM standard 5-mm subsized Charpy V-notch specimens from Series III, IV and V weld metal. The transition curves obtained by plotting all available data for 1.2-, 2.5- and 3.7-MJ/m (30-, 64- and 94-kJ/in.) heat inputs are shown in Figs. 3A, B and C, respectively. There is limited scatter in the data in Figs. 3A, B and C. All welds exhibited a transition from ductile to brittle fracture behavior over the test temperature range investigated. The Series III 1.2-MJ/m weld shows a narrow ductile-to-brittle transition behavior (see Fig. 3A), while the transitions from the upper shelf to the lower shelf for the 2.5-MJ/m and 3.7-MJ/m welds are gradual and occur